Journal of Power Sources 279 (2015) 394–404

Contents lists available at ScienceDirect

Journal of Power Sources

journal homepage: www.elsevier.com/locate/jpowsour

Highly selective hydrogenation of CO_2 to methanol over CuO–ZnO–ZrO_2 catalysts prepared by a surfactant-assisted co-precipitation method

Li Li, Dongsen Mao*, Jun Yu, Xiaoming Guo

Research Institute of Applied Catalysis, School of Chemical and Environmental Engineering, Shanghai Institute of Technology, Shanghai 201418, PR China

HIGHLIGHTS

- CuO/ZnO/ZrO_2 catalyst was prepared by a surfactant-assisted coprecipitation method.
- The methanol yield increases with the S_{Cu} but it is not a linear relationship.
- TOF for methanol formation decreases with the enlargement of Cu particles.
- High methanol selectivity is due to more Cu-support species and mesopores.

ARTICLE INFO

Article history:
Received 12 August 2014
Received in revised form
2 December 2014
Accepted 29 December 2014
Available online 30 December 2014

Keywords:
CuO–ZnO–ZrO_2 catalyst
Surfactant-assisted co-precipitation
CO_2 hydrogenation
Methanol synthesis

ABSTRACT

A series of CuO–ZnO–ZrO_2 catalysts are synthesized by a surfactant-assisted co-precipitation method and tested for the synthesis of methanol from CO_2 hydrogenation. The effects of calcination temperature on the physicochemical properties of as-prepared catalysts are investigated extensively by TG-DSC, N_2 adsorption/desorption, XRD, N_2O chemisorption, SEM/TEM, EDX, XPS, TPR, H_2-TPD and CO_2-TPD techniques. The results show that the size of copper particles increases with the increase in calcination temperature, leading to the decrease in turnover frequency (TOF) for methanol formation. Moreover, compared with the counterparts prepared by the conventional co-precipitation method, the CuO–ZnO–ZrO_2 catalysts prepared by this novel method show significantly high methanol selectivity. The superior property of the prepared CuO–ZnO–ZrO_2 catalyst can be attributed to the formation of more amounts of Cu–ZnO_x and/or Cu–ZrO_x species resulted from the homogeneous element distribution, intimate interface contact of Cu species with ZnO and/or ZrO_2, and to porous structure with larger pore size.

1. Introduction

It is well known that CO_2 is not only the most important greenhouse gas, but also a significant carbon resource which is low-cost, non-toxic and easily achievable. With the increase in CO_2 concentration in the atmosphere, and the depletion of fossil fuels, conversion of CO_2 to useful chemicals and fuels may be one of the most promising ways to liberate mankind from this awkward situation [1]. Most of the present research focuses on CO_2 hydrogenation to methanol because methanol is an important feedstock for the chemical industry and a potential alternative to fossil fuels. Furthermore, the convenient production of H_2 at large scale from renewable energy sources such as solar energy, hydropower and biomass also supports this green process [2]. Based on the great significance of methanol synthesis from CO_2 hydrogenation, a new concept of "methanol economy" was proposed by Olah et al. [2,3].

The majority of research on CO_2 hydrogenation to methanol was conducted over Cu–ZnO–Al_2O_3 catalyst which has been widely used for methanol synthesis from syngas (H_2 + CO) containing small amount of CO_2. However, the Cu–ZnO–Al_2O_3 catalyst performed not perfectly in CO_2 hydrogenation, which can be ascribed to the negative effect of water on the rate of methanol formation and the stability of active sites, and the strong hydrophilic characteristic of alumina [4–6]. On the other hand, Cu–ZrO_2 or modified Cu–ZrO_2 catalysts have gained an increasing interest for their high activity in methanol synthesis from CO_2 hydrogenation due to the high thermal stability of ZrO_2 under reducing and oxidizing conditions [7] and the promotional effect of ZrO_2 on the reduction

* Corresponding author.
E-mail address: dsmao@sit.edu.cn (D. Mao).

http://dx.doi.org/10.1016/j.jpowsour.2014.12.142
0378-7753/

of oxidized CuO_x [6]. Among them, Cu–ZnO–ZrO_2 catalyst is particularly effective for the synthesis of methanol from CO_2 hydrogenation [5–27]. In order to further improve the performance of Cu–ZnO–ZrO_2 catalyst, the addition of promoters such as Mn [9,10,19,20], Ga [7,9,18], Mg [9,10,19], Y [9], La [23,24] and Ce [25] have been reported recently. Apart from catalyst composition, preparation methods and conditions also have a considerable influence on the performance of Cu–ZnO–ZrO_2 catalyst [8–11,27]. Up to now, such methods as co-precipitation [6–8,11–18,25–27], thermal decomposition of citrate [9,10,17,18,26] and sol–gel [21,22] have been developed to prepare CuO–ZnO–ZrO_2 catalyst. Very recently, solution combustion [28–30] and solid-state chemical reaction [31] syntheses were found to be simple and effective methods for the preparation of CuO–ZnO–ZrO_2 catalyst. However, the catalysts prepared by the above two methods are found to be with lower BET surface areas, which is disadvantageous for the catalytic activity [32]. For example, the highest BET surface area of CuO–ZnO–ZrO_2 catalysts prepared by glycine-nitrate combustion method was <20 m^2/g [29]. Therefore, the development of new methods for preparing highly effective CuO–ZnO–ZrO_2 catalyst is imperative and significant.

In recent years, a new method involving a surfactant in the precipitation process was reported, and the obtained catalysts show relatively high specific surface areas and improved catalytic behavior. For instance, CuO–CeO_2 catalysts with large surface areas and worm-like mesoporous structures were prepared using cetyltrimethyl ammonium bromide (CTAB) as the template and NaOH as the precipitating agent; and this material showed high activity for CO oxidation [33,34], selective catalytic oxidation of ammonia [35], and catalytic destruction of 1,2-dichlorobenzene [36]. Likely, mesoporous CuO–Fe_2O_3 [37], CuO/$Ce_{0.8}Zr_{0.2}O_2$ [38], CuO/$Ti_xZr_{1-x}O_2$ [39], and CuO/$Ti_{0.8}Ce_{0.2}O_2$ [40] were also synthesized by using the same method, which exhibited high catalytic activity for CO oxidation. Nonetheless, there isn't any report about preparing Cu-based catalysts following this method for CO_2 hydrogenation, to the best of our knowledge.

In this work, mesoporous CuO–ZnO–ZrO_2 composite oxides with uniform pore-size distributions were synthesized by a surfactant-assisted co-precipitation method using CTAB as template, and used as catalysts for methanol synthesis from CO_2 hydrogenation. The structural and textural properties of the prepared CuO–ZnO–ZrO_2 catalysts were characterized intensively by TG-DSC, XRD, N_2 adsorption/desorption, XPS, SEM/TEM, EDX, TPR, and TPD techniques. Since calcination temperature is an important parameter in catalyst preparation by co-precipitation method, the effects of different calcination temperatures on the physicochemical and catalytic properties of the CuO–ZnO–ZrO_2 was investigated. For comparison, CuO–ZnO–ZrO_2 catalysts of the same composition were also prepared by the conventional co-precipitation method. Furthermore, the catalytic performances of the catalysts were discussed deeply in relation to the results of physicochemical characterizations.

2. Experimental

2.1. Catalyst preparation

The CuO–ZnO–ZrO_2 catalysts were prepared by using a surfactant-assisted co-precipitation method, in which the molar ratio of Cu^{2+}:Zn^{2+}:Zr^{4+} = 5:2:3 was chosen based on our previous studies [28–31]. All chemicals were of analytical grade and used as received (Shanghai Chemical Reagent Corporation, PR China) without further purification. In a typical procedure, 6 mmol of CTAB was dissolved into 200 mL distilled water, followed by ultrasound irradiation for 15 min. Then, 5 mmol of $Cu(NO_3)_2 \cdot 3H_2O$, 2 mmol of $Zn(NO_3)_2 \cdot 6H_2O$ and 3 mmol of $Zr(NO_3)_4 \cdot 5H_2O$ were added under magnetic stirring. After stirring for 0.5 h, a NaOH solution (0.2 mol/L) was added into the above solution until the pH value of the mixture was 10 ± 0.2, and then further stirred for about 12 h. The obtained suspension was further hydrothermally aged at 90 °C for 3 h. The final precipitate was filtered, washed with hot distilled water, dried in the oven at 110 °C for 12 h, and then milled to obtain the precursor. In order to investigate the influence of calcination temperature, the CuO–ZnO–ZrO_2 catalysts were obtained by calcining the precursor at 300–600 °C for 5 h in a muffle oven and designated as S-CZZ-300, S-CZZ-400, S-CZZ-500, and S-CZZ-600, respectively. In addition, for comparison, the samples which followed the above steps, while without adding CTAB were prepared and designated as CZZ-300, CZZ-400, CZZ-500, and CZZ-600, respectively.

2.2. Catalyst characterization

The thermal gravimetric and differential scanning calorimetry (TG-DSC) analyses of the dried samples prior to calcination were conducted on a thermal analyzer (SAT 449 F3, NETZSCH) at a heating rate of 10 °C/min under a continuous-flow of air.

X-ray diffraction (XRD) patterns were recorded with a PANalytical X'Pert diffractometer operating with Ni β-filtered Cu K_α radiation at 40 kV and 40 mA. Two theta angles ranged from 10° to 80° with a speed of 6° per minute.

BET surface area and pore size distribution were measured on a Micromeritics ASAP2020M + C adsorption apparatus at liquid N_2 temperature using N_2 as adsorbate. Before measurements, the samples were dried in situ at 200 °C for 4 h under vacuum.

The surface morphology was observed by the scanning electronic microscopy (SEM, S-3400 N, Hitachi) and transmission electron microscopy (TEM, TECNAI). The bulk element compositions of the samples were determined by using an energy dispersive X-ray spectrometer (EDX) (X Flash Detector 4010). The metallic copper surface area (S_{Cu}) in the reduced catalyst was determined by using a N_2O chemisorption method similar to that described by Chinchen et al. [41]. Once the catalyst was reduced in a 10 vol% H_2/He mixture at 300 °C for 1 h, it was exposed to a flow of He and cooled to the chemisorption temperature (60 °C). Then, a flow of 1 vol% N_2O/He gas mixture was fed into the reactor. The N_2 produced by the decomposition of N_2O on the exposed Cu atoms was detected using a mass spectrometer (Pfeiffer Vacuum Quadstar, 32-bit). The metallic copper surface area was calculated assuming an atomic copper surface density of 1.46×10^{19} Cu atoms/m^2 and a molar stoichiometry of $N_2O/Cu = 0.5$ [14].

X-ray photoelectron spectroscopy (XPS) measurements were performed on a Kratos Axis Ultra DLD spectrometer equipped with an Al K_α (1486.6 eV) X-ray exciting source. The pass energy of the analyzer was set at 40 eV. The binding energies were referenced to the adventitious C 1s peak at 284.6 eV (accuracy within ±0.1 eV).

Temperature-programmed reduction (TPR) measurements were performed in a continuous-flow apparatus fed with a 10% H_2/N_2 mixture flowing at 30 mL/min and heated at a rate of 5 °C/min. A 30-mg sample was used, with H_2 consumption monitored by a thermal conductivity detector (TCD).

Hydrogen temperature-programmed desorption (H_2-TPD) was carried out in a quartz tubular reactor. Firstly, the catalyst was reduced at 300 °C for 1 h in a flowing of 10% H_2/N_2 mixture. Then the sample was cooled to room temperature and further saturated in H_2/N_2 mixture for 1 h, followed by flushing in N_2 for 1 h. The TPD measurements were conducted in a N_2 stream (30 mL/min) from room temperature to 500 °C at a heating rate of 5 °C/min. The change of hydrogen signal was monitored by a TCD and quantitatively calibrated by H_2 pulses.

The basicity of the catalyst was measured by CO_2 temperature-programmed desorption (CO_2-TPD). Prior to the adsorption of CO_2, the catalyst sample was reduced at 300 °C for 1 h in a flowing of 10% H_2/N_2 mixture, followed by flushing in N_2 for 1 h. After cooling to room temperature, the catalyst was saturated with a 10% CO_2/N_2 mixture (30 mL/min) at 60 °C for 1 h. Afterwards, the TPD experiment was started with a heating rate of 10 °C/min under N_2 flow (30 mL/min), and the desorbed CO_2 was detected by a mass spectrometer (Pfeiffer Vacuum Quadstar, 32-bit). The amount of the desorbed CO_2 was quantified by comparing the integrated area of the TPD curve to the peak area of the injected CO_2 calibration pulse.

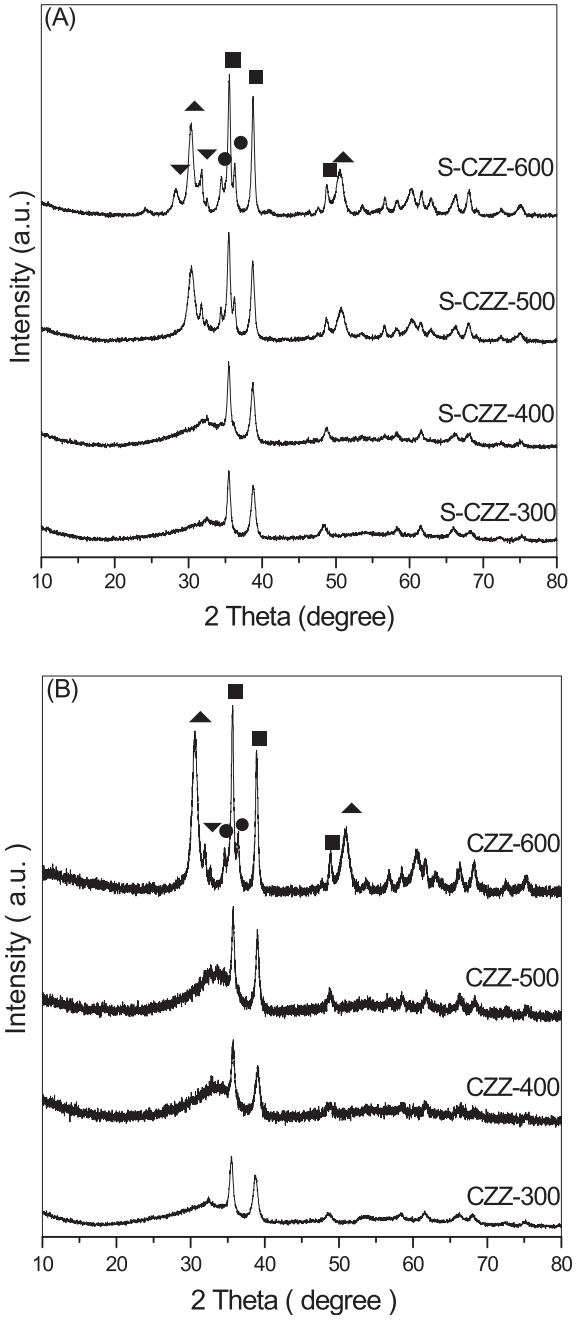

Fig. 1. XRD patterns of the different CuO–ZnO–ZrO_2 catalysts: (A) S-CZZ and (B) CZZ (■) CuO; (●) ZnO; (▲) ZrO_2 (tetragonal); (▼) ZrO_2 (monoclinic).

2.3. Catalyst testing

Activity and selectivity measurements for CO_2 hydrogenation were carried out in a continuous-flow, fixed-bed reactor. About 0.5 g of catalyst diluted with quartz sand (both in 20–40 mesh) was packed into the stainless steel tubular reactor (5 mm i.d.). Preliminary experiments with respect to possible influence caused by interparticle mass transfer limitation confirmed that such limitation could be ruled out under the conditions used in the present study. Prior to the catalytic measurement, the fresh catalyst was reduced in a stream of 10% H_2/N_2 flowing at 30 mL/min at 300 °C for 3 h under atmospheric pressure. Then the reactor was cooled to a given temperature and a gas mixture (CO_2:H_2:N_2 = 22:66:12, molar ratio) was introduced, raising the pressure to 3.0 MPa. All post-reactor lines and valves were heated to 170 °C to prevent product condensation. Effluent products were analyzed on-line with a gas chromatograph (6820, Agilent) equipped with two columns: Porapak Q column connected to a flame ionization detector (FID) for methanol and Carbosieve column to a TCD for other gaseous products. Conversion and selectivity values were calculated according to Eqs. (1)–(3) and the steady-state values were quoted as the average of four different analyses taken after 5 h on stream operation.

$$X_{CO_2}\% = \frac{A'_{CO}\cdot f_{CO} + A'_{CH_3OH}\cdot f_{CH_3OH}}{A'_{CO}\cdot f_{CO} + A'_{CH_3OH}\cdot f_{CH_3OH} + A'_{CO_2}\cdot f_{CO_2}} \times 100 \quad (1)$$

$$S_{CO}\% = \frac{A'_{CO}\cdot f_{CO}}{A'_{CO}\cdot f_{CO} + A'_{CH_3OH}\cdot f_{CH_3OH}} \times 100 \quad (2)$$

$$S_{CH_3OH}\% = \frac{A'_{CH_3OH}\cdot f_{CH_3OH}}{A'_{CO}\cdot f_{CO} + A'_{CH_3OH}\cdot f_{CH_3OH}} \times 100 \quad (3)$$

where, A_i represent the integral peak areas of products (CO and methanol) or CO_2 in the GC analysis, and f_i represent their correction factors.

3. Results and discussion

3.1. Catalyst characterization

3.1.1. XRD

Fig. 1 shows the XRD patterns of the S-CZZ and CZZ catalysts calcined at different temperatures. As seen in Fig. 1(A), when the calcination temperature is low (300 or 400 °C), only the diffraction lines of CuO (JCPDS 80–1268) are observed at 2θ of 35.6, 38.8 and 48.9°; while the diffraction peaks of ZnO and ZrO_2 cannot be observed, suggesting that they may exist in an amorphous state or have been highly dispersed so that their particles are too small to be identified by the conventional X-ray diffraction method. Increasing the calcination temperature to 500 °C, the diffraction peaks of CuO become stronger and sharper, indicating an increase in the crystallization degree of CuO and the growth of CuO nanoparticles. Moreover, there are the diffraction lines of ZnO phase (JCPDS 36–1451) appearing at 2θ of 34.5 and 36.3°, together with the diffraction lines of both tetragonal zirconia (t-ZrO_2, 2θ = 30.3, 50.7°, JCPDS 88–1007) and monoclinic ZrO_2 (m-ZrO_2, 2θ = 31.5°, JCPDS 83–0940). When the calcination temperature is further raised to 600 °C, the diffraction peaks for CuO, ZnO and ZrO_2 become sharper and stronger, indicating an increase in the degree of crystallinity and in the particle sizes of CuO, ZnO and ZrO_2 crystallites. Furthermore, another peak of m-ZrO_2 appears at 2θ = 28.2°(JCPDS 83–0940), and the intensity of m-ZrO_2 peak at 2θ = 31.5° increases,

confirming that the partial transformation of ZrO_2 phase from tetragonal to monoclinic occurs with increasing the calcination temperature [31]. The crystallite size of CuO, which is estimated using the Scherrer equation, increases noticeably from 18.2 nm of S-CZZ-300 to 23.9 nm of S-CZZ-600, as shown in Table 1.

For the CZZ catalysts (Fig. 1(B)), no other diffraction peaks except those of CuO could be observed when the calcination temperature is ≤500 °C, indicating that the ZnO and ZrO_2 exist in an amorphous state or have been highly dispersed on these catalysts. When the calcination temperature is increased to 600 °C, the diffraction peaks for ZnO and ZrO_2 appear. Compared with the counterpart S-CZZ-600, however, the peak of *m*-ZrO_2 at $2\theta = 28.2°$ cannot be observed and the intensity of the diffraction lines of *t*-ZrO_2 is significantly stronger on the CZZ-600 catalyst. On the other hand, the diffraction peaks of CuO in CZZ series samples are slightly broader, which is in agreement with the fact that the crystallite sizes of CuO of the CZZ samples (17.1–21.7 nm) are slightly smaller than those of CuO of the corresponding S-CZZ samples (18.2–23.9 nm), as shown in Table 1. These results suggest that the addition of CTAB promotes the crystallization of CuO, ZnO and ZrO_2, and the transformation of ZrO_2 phase from tetragonal to monoclinic.

Fig. 2 shows the XRD patterns of different Cu–ZnO–ZrO_2 catalysts after in situ reduced in H_2 at 300 °C. As seen, all the catalysts exhibit three diffraction peaks at 2θ of 43.3, 50.5, and 73.7° characteristic of the Cu (111), Cu (200) and Cu (220) planes, respectively [42]; and the diffraction lines of CuO completely disappear, indicating that the CuO in the samples are totally reduced to metallic copper. As shown in Table 1, the change trend for crystallite size of Cu over the reduced catalysts is the same as that for crystallite size of CuO over the calcined catalysts. Furthermore, the transformation of ZrO_2 phase with the increase in calcination temperature is also the same as that observed in Fig. 1.

3.1.2. N_2 adsorption-desorption

Figs. 3 and 4 respectively depict the N_2 adsorption–desorption isotherms and the corresponding pore size distributions of the different CuO–ZnO–ZrO_2 catalysts; and their textural properties are summarized in Table 1. As seen in Fig. 3(A), the isotherms of all the prepared S-CZZ series samples are of classical type IV, characteristic of mesoporous materials accorded to the IUPAC. The well-defined hysteresis loops with a steep desorption branch and a less steep adsorption branch belong to the H2-type, indicating that the effective radii of the mesoporous bodies are heterogeneously distributed and the effective radii of the narrow entrances are all of equal size [43]. The H2 type of hysteresis loop is typical for wormhole-like mesostructures and hierarchical scaffold-like mesoporous structures formed by surfactant-assisted nanoparticle assembly [43,44]. The pore size distribution curves of the S-CZZ series catalysts calcined at different temperatures, determined by the BJH method from the adsorption branch of the isotherms, exhibit one single narrow peak centered at 2.4–8.2 nm, and the pore sizes enlarge with the increase in calcination temperature (Fig. 4(A)).

As shown in Table 1, with the increase in calcination temperature, the surface area of the S-CZZ catalysts decreases from 116.5 to 25.0 m^2/g, accompanied by the decrease in the pore volume. This can be ascribed to the increase in the degree of crystallinity and the agglomeration of CuO, ZnO and ZrO_2 nanoparticles as evidenced by

Table 1
Textural and structural properties of the different CuO–ZnO–ZrO_2 catalysts.

Catalyst	S_{BET} (m^2/g)	Pore volume[a] (cm^3/g)	Pore diameter[b] (nm)	d^c_{CuO} (nm)	d^d_{Cu} (nm)	S^e_{Cu} (m^2/g)
S-CZZ-300	116.5	0.150	2.4	18.2	16.5	3.28
S-CZZ-400	95.2	0.144	2.7	19.6	18.3	3.21
S-CZZ-500	51.8	0.133	4.3	20.7	18.5	3.12
S-CZZ-600	25.0	0.113	8.2	23.9	19.8	2.96
CZZ-300	121.1	0.100	1.2	17.1	15.9	3.85
CZZ-400	99.4	0.098	1.4	18.9	17.9	3.68
CZZ-500	56.2	0.091	1.9	20.0	18.2	3.59
CZZ-600	28.8	0.059	4.9	21.7	19.4	3.09

[a] Total pore volume at $P/P_0 = 0.99$.
[b] Maximum of BJH pore diameter as determined from the adsorption branch.
[c] Determined from full width at half maxima of CuO (111) XRD peak.
[d] Determined from full width at half maxima of Cu (111) XRD peak.
[e] Determined by N_2O chemisorption method.

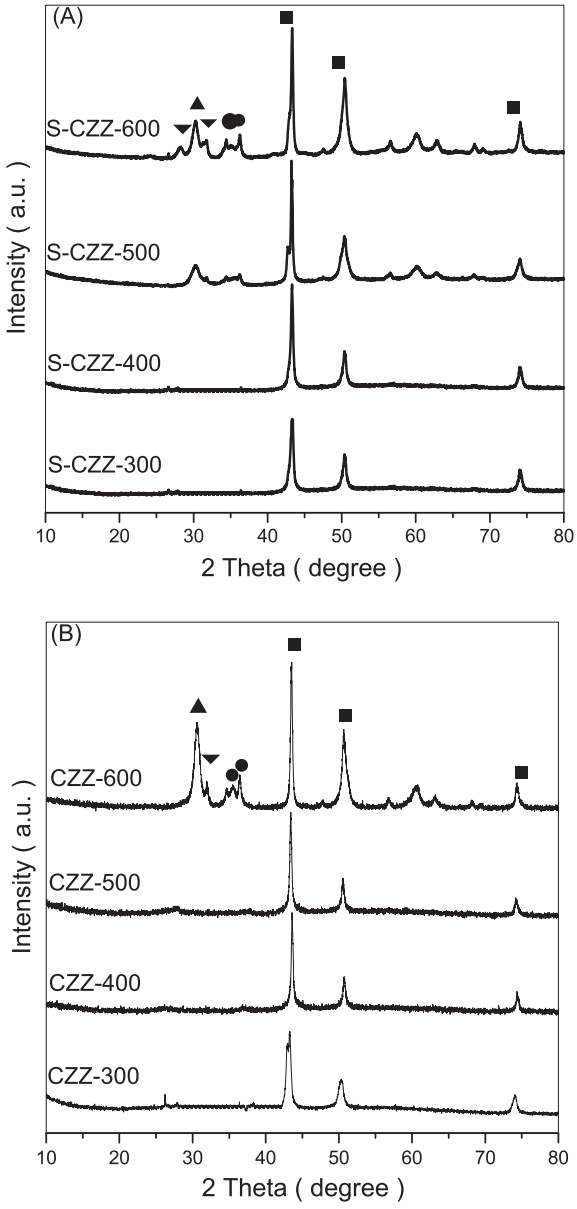

Fig. 2. XRD patterns of the different Cu–ZnO–ZrO_2 catalysts after in situ reducing at 300 °C: (A) S-CZZ and (B) CZZ (■) Cu; (●) ZnO; (▲) ZrO_2 (tetragonal); (▼) ZrO_2 (monoclinic).

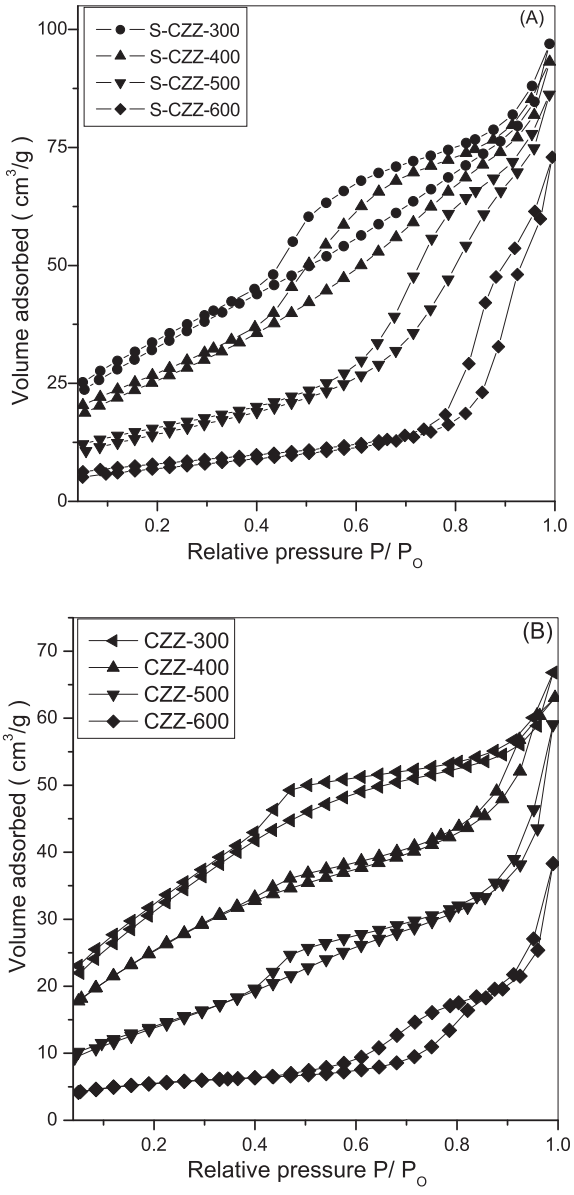

Fig. 3. N_2 adsorption–desorption isotherms of the different CuO–ZnO–ZrO_2 catalysts: (A) S-CZZ and (B) CZZ.

the XRD results described above.

For the reference CZZ series samples, the H2 type of hysteresis loop (Fig. 3(B)) is rather small, indicating that the mesoporous structure is not existing significantly. Furthermore, it can be seen from Fig. 4(B) and Table 1 that the pore diameters of the CZZ series samples except CZZ-600 are only 1.2–1.9 nm, which indicates that they are mainly microporous materials. As shown in Table 1, both the surface areas and pore volumes of the CZZ catalysts decrease with the increase in calcination temperature due to the same reason as described above for the S-CZZ catalysts. On the other hand, compared with the corresponding S-CZZ catalysts, the CZZ catalysts exhibit similar surface areas but evidently low pore volumes, indicating that the S-CZZ catalysts prepared by the surfactant-assisted co-precipitation method possess significantly higher porosity.

3.1.3. TG-DSC

The TG-DSC patterns of the precursor of CuO–ZnO–ZrO_2 catalyst prepared by the surfactant-assisted co-precipitation method before calcination are shown in Fig. 5(A). It is clear that a continuous weight loss occurs from room temperature to about 650 °C. The process of weight loss can be divided into three steps. A small endothermic peak in the temperature range of 100–150 °C on DSC, accompanied by 2% of the weight loss observed in this first step on TG curve, is attributed to the desorption of adsorbed water that may be physical or chemical adsorption on the surface of the sample or resides in the mesopores. The second step on TG curve from 150 to 620 °C with a main weight loss of about 7.17%, accompanied with a sharp exothermic peak at 337 °C and a broad exothermic peak at 350–620 °C, can be attributed to the combined effect from both of the residual surfactant decomposition and partial de-hydroxylation being converted into oxides on the surface. The third step on DSC curve with a sharp exothermic peak at 648 °C and with no weight loss on TG curve can be attributed to the transformation of ZrO_2 phase from tetragonal phase to monoclinic phase.

Compared with the precursor of the S-CZZ catalysts, the TG-DSC patterns of the precursor of the CZZ catalysts (Fig. 5(B)) exhibit a

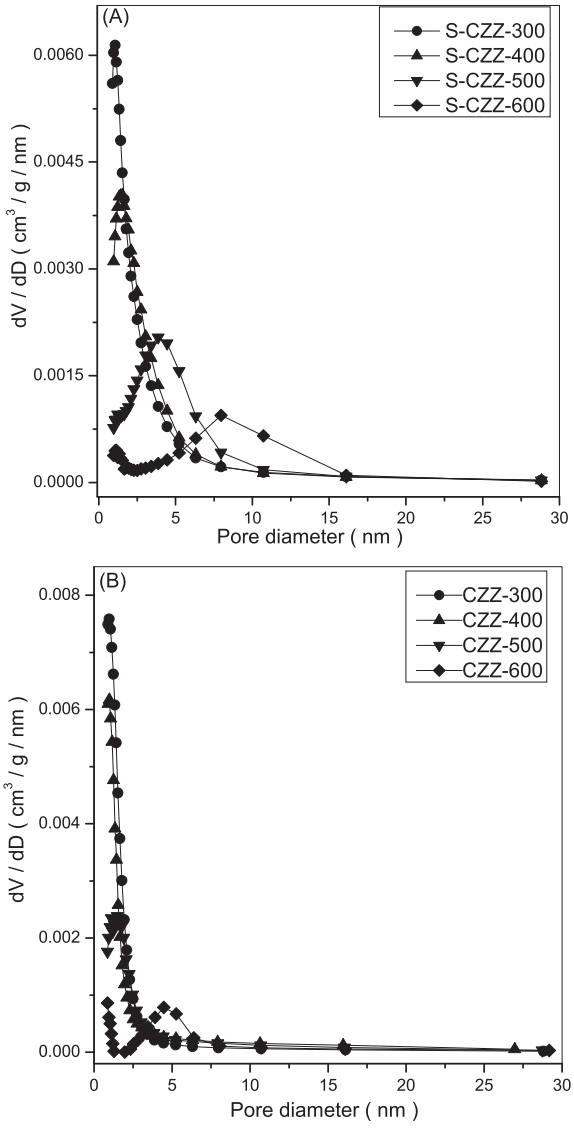

Fig. 4. The pore size distributions of the different CuO–ZnO–ZrO_2 catalysts: (A) S-CZZ and (B) CZZ.

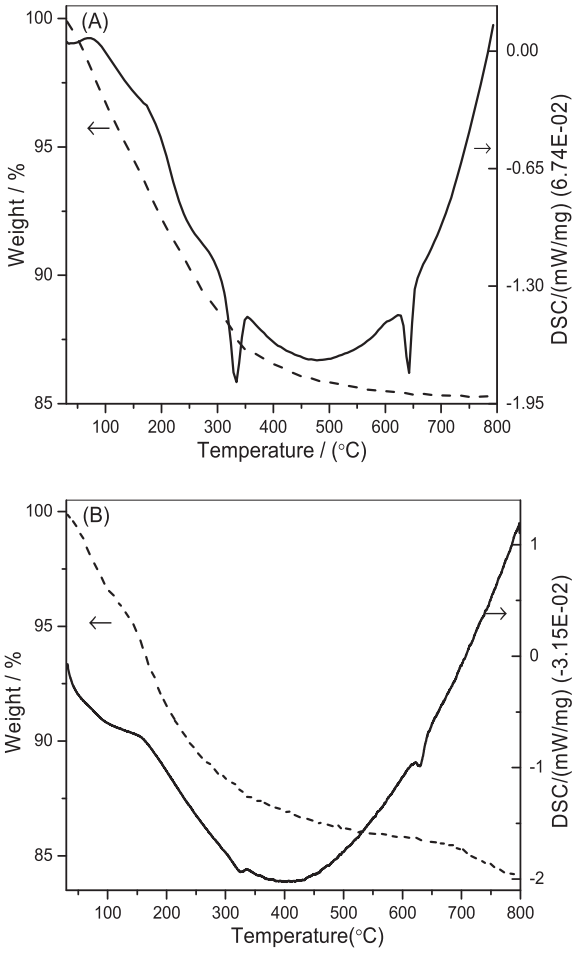

Fig. 5. The TG-DSC patterns of the precursors of the different CuO–ZnO–ZrO_2 catalyst: (A) S-CZZ and (B) CZZ.

smaller weight loss and a weaker exothermic peak at about 335 °C, which can be assigned to the absence of the residual surfactant decomposition. Moreover, the exothermic peak at about 650 °C which is attributed to the transformation of ZrO_2 phase from tetragonal phase to monoclinic phase is remarkably weaker; this result indicates a lesser extent of the transformation of ZrO_2 phase, which is in line with that obtained by XRD analyses described above.

3.1.4. SEM/TEM and EDX

SEM micrographs (not shown here) of the samples show that all the CuO–ZnO–ZrO_2 catalysts are in the form of irregular particles. Nevertheless, with increasing the calcination temperature, the aggregation trend of the particles of both the S-CZZ and CZZ series catalysts becomes stronger which should probably be due to the particle sintering after treatment at higher temperatures. On the other hand, there is little difference between the S-CZZ and CZZ series catalysts, indicating that the addition of CTAB in the co-precipitation process does not induce noticeable difference in morphology and particle size of the CuO–ZnO–ZrO_2 catalysts.

Fig. 6 shows the TEM images of the representative CZZ-300 and S-CZZ-300 samples. It can be seen that individual separated oxide particles are observed for the CZZ-300 sample with the sizes of 10–20 nm. Unlike the sample CZZ-300, individual separated oxide particles are not easily distinguished on the sample S-CZZ-300. The CuO particles are partially embedded in the oxide matrix with an intimate interface contact with the surrounding matrix Cu-depleted oxide. A similar phenomena is also reported by Behrens et al. [45] who prepared the CuO/ZnO/Al_2O_3 catalyst by a modified co-precipitation method using a combination of sodium aluminate and carbonate solution as precipitating agent for a Cu,Zn-nitrate solution during co-precipitation and direct spray-drying of the fresh precipitate suspension.

During the preparation of the CuO–ZnO–ZrO_2 catalysts, the initial molar ratio of copper, zinc and zirconium in the solution is 5:2:3. The addition of CTAB promotes the aggregation and precipitation of precursor sol particles. If the deposition rates of copper, zinc and zirconium precursors are different, the Cu/Zn/Zr atomic ratio in the resulted precipitates might not be 5:2:3 [46]. For identification purpose, the bulk element compositions of the calcined CuO–ZnO–ZrO_2 samples are analyzed by EDX technique and the results are shown in Table 2. It can be seen that, for all the samples, only copper, zinc, zirconium, oxygen and carbon elements are detected and the Cu/Zn/Zr atomic ratios of the S-CZZ series samples determined by chemical analysis are in close agreement with the nominal ratio (5:2:3) taken for the catalyst preparation. This result indicates that the copper, zinc and zirconium precursor sol in the solution are precipitated simultaneously after CTAB being added. On the contrary, the determined ratios of the reference CZZ series samples except CZZ-600 are evidently deviated from the nominal data, i.e. with higher contents of Cu and lower contents of Zr, indicating that more copper is precipitated at the expense of zirconium. On the other hand, the content of carbon of the S-CZZ series samples decreases continuously with the increase in calcination temperature, which results from the effective elimination of surfactant resides in the catalyst.

3.1.5. N_2O titration and XPS analysis

The metallic copper surface areas (S_{Cu}), which are determined by N_2O titration, of all the CuO–ZnO–ZrO_2 samples are also presented in Table 1. It can be seen that the S_{Cu} of both the S-CZZ and CZZ series samples decreases with the increase in calcination temperature. Because the value of S_{Cu} is a mirror of the dispersion of Cu, it can be concluded that the dispersion of Cu on the both series samples decreases with the calcination temperature increasing. Moreover, the S_{Cu} values of the CZZ series samples are slightly larger than those of the corresponding S-CZZ series samples due to the relatively smaller size of Cu as determined by the in situ XRD technique (Table 1).

Surface compositions of the representative samples determined by the XPS method are shown in Table 3. As seen, the Cu contents on the surface of S-CZZ-300 and S-CZZ-600 samples are smaller than those on the surface of the corresponding samples CZZ-300 and CZZ-600. This result is in accordance with the smaller Cu surface areas of S-CZZ-300 and S-CZZ-600 samples measured by N_2O titration (Table 1). Moreover, the surface Cu contents of both S-CZZ and CZZ series samples decrease drastically with the increase in calcination temperature. A similar result is also found previously over the CuO–ZnO–ZrO_2 catalysts prepared by a route of solid-state reaction and calcined at different temperatures [31]. Moreover, the relative Cu/Zn/Zr molar ratios of the four samples are also included in Table 3. Compared with the bulk element compositions (Table 2), there exists distinct difference between the surface and bulk. Particularly, for the two series of catalysts CZZ-300 and S-CZZ-300, CZZ-600 and S-CZZ-600 which calcined at the same temperatures, noticeably higher Cu/Zn molar ratio values are found for the CZZ samples compared with those for the S-CZZ samples (~2.7 vs. ~1.1 for CZZ-300 and S-CZZ-300, and ~1.2 vs. ~0.85 for CZZ-600 and S-CZZ-600, respectively.)

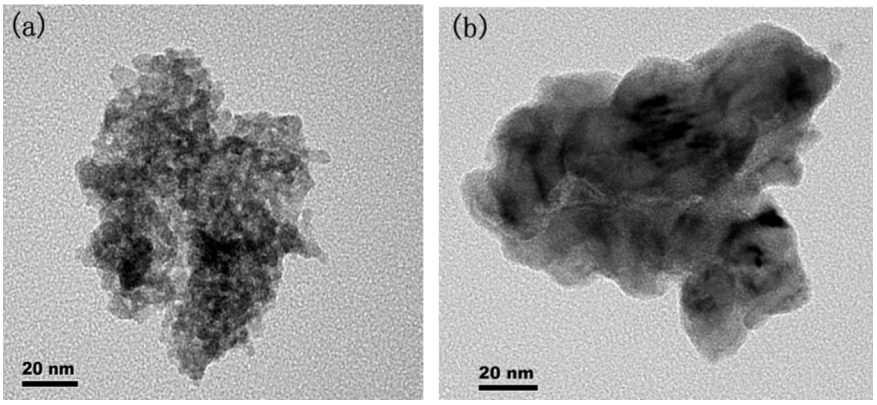

Fig. 6. TEM images of CZZ-300 (a) and S-CZZ-300 (b).

3.1.6. The reducibility of the catalysts

To assess the reduction behavior of the catalysts, TPR measurements were performed. Fig. 7 shows the H_2-TPR profiles of the studied samples. Since ZnO and ZrO_2 are not reduced within the experimental regions [47–49], the reduction peaks are related to the reduction of different CuO species. As noted from Fig. 7(A), a very broad peak is observed for the catalysts S-CZZ-300, S-CZZ-400 and S-CZZ-500. Furthermore, the position of the peak shifts to higher temperatures with the calcination temperature increasing, indicating that the sizes of CuO domains increase from S-CZZ-300 to S-CZZ-500 because the higher the reduction temperature is, the larger the CuO particle will be [50]. This result is in good line with that obtained by XRD analysis (Table 1). However, at least two overlapped reduction peaks are observed with the sample S-CZZ-600, suggesting that there are two kinds of CuO-related species. As well documented, the low temperature peak (α peak) is attributed to the reduction of highly dispersed CuO surface species interacting with ZnO and ZrO_2; whereas the peak appearing at higher temperature (β peak) is related to the reduction of the uninteracted or bulk-like CuO species [49–51]. Furthermore, there is no notable difference between the integrated areas of the TPR peaks over the different S-CZZ samples, suggesting that the total hydrogen consumption is basically equal. A similar phenomenon is also found previously over the CuO–ZnO–ZrO_2 catalysts prepared by a route of solid-state reaction and calcined at different temperatures [31].

Compared with the S-CZZ series catalysts, two well-resolved peaks are observed for all the CZZ series catalysts, illustrating that two types of CuO species coexist on their surfaces as described above. On the other hand, the positions of reduction peaks of the CZZ series catalysts shift towards lower temperatures, indicating that the particle sizes of CuO are smaller on the CZZ series catalysts. This result is in good agreement with those obtained by XRD and N_2O titration techniques (Table 1). Therefore, it should be noted that the calcination temperature during the thermal treatment process and that the addition of CTAB during the co-precipitation process affect greatly the reduction ability of CuO–ZnO–ZrO_2 catalysts. That is to say, higher calcination temperatures may cause the sintering of CuO particles, while the addition of CTAB improves the interaction of CuO with ZnO and ZrO_2.

3.1.7. H_2-TPD analysis

The H_2-TPD profiles for the pre-reduced catalysts are presented in Fig. 8. Two desorption peaks can be observed for all the catalysts investigated here. The low temperature peak (peak α) located in the temperature range of 72–86 °C represents the desorption of atomic hydrogen on the surface of metallic Cu [14], while the high temperature peak (peak β) centered at about 385 °C is due to the desorption of strongly adsorbed hydrogen over bulk CuO and ZnO or ZrO_2 surface [52,53]. The maximum desorption temperature (T_{max}) and the quantitative data of the amounts of desorbed H_2 are listed in Table 4. It can be seen that, with the calcination temperature increasing, the position of the peak α for both series catalysts shifts to lower temperatures, accompanied by the decreasing area for H_2-desorption. This result indicates that the amounts of H_2 desorbed from Cu sites reduced with the calcination temperature elevating. This is in line with the variation trend of S_{Cu} (Table 1). On the other hand, the position of the peak β remains constant, while the amounts of desorbed H_2 decrease monotonously and slightly with the increase in calcination temperature due to the sintering of CuO, ZnO and ZrO_2 (as seen from XRD and H_2-TPR results). The better adsorption strength of H_2 molecular and the dissociated atomic hydrogen is beneficial to the hydrogenation of activated CO_2 species to form methanol [54]. On the other hand, it should be emphasized that only the H_2 desorbed at lower temperature is useful for the synthesis of methanol from CO_2 hydrogenation since the reaction usually takes place below 623 K [23]. This inference was confirmed by the catalytic activity of different catalysts as described in Section 3.2.

Compared with the S-CZZ series samples, the position of peak α shifts slightly to a lower temperature and that of peak β remains constant basically over the corresponding CZZ series samples (Table 4). On the other hand, the areas of both α and β peaks are almost the same for the two series samples calcined at the same temperatures. This result suggests that the addition of CTAB during the co-precipitation process has negligible effect on the hydrogen adsorption of the Cu–ZnO–ZrO_2 catalysts.

3.1.8. The basicity of catalysts

Fig. 9 shows the CO_2 desorption profiles obtained for the pre-reduced Cu–ZnO–ZrO_2 catalysts. Two CO_2 desorption peaks can be observed for all the samples. The low temperature peak (peak α) represents a weak basic site, while the high temperature peak (peak β) corresponds to a strong basic site. As shown in Fig. 9, the differences of the positions of these desorption peaks are very small for all the samples, suggesting that there is no significant change of the strength of basic sites with the different calcination temperatures during the thermal treatment process for the two series samples. However, with the calcination temperature rising, the areas of both α and β peaks for the two series samples decrease markedly, which indicates that the amounts of both weak and strong basic sites decline with the increase in calcination temperature. The decrease in basicity is unfavorable for the adsorption of acidic CO_2 and ultimately decreases the activity [51].

On the other hand, the areas and the positions of both peak α

Table 2
The bulk element compositions of the different CuO–ZnO–ZrO_2 catalysts.

Catalyst	Cu (wt %)	Zn (wt %)	Zr (wt %)	O (wt %)	C (wt %)	Cu/Zn/Zr molar ratio
S-CZZ-300	34.0	13.2	27.9	22.3	2.7	5.1:1.9:3.0
S-CZZ-400	33.8	13.2	28.8	22.3	2.0	5.0:1.9:3.1
S-CZZ-500	33.5	14.0	28.9	22.3	1.3	5.0:1.9:3.1
S-CZZ-600	29.7	13.0	29.2	27.6	0.5	4.8:2.0:3.2
CZZ-300	36.4	13.9	21.8	28.0	–	5.6:2.1:2.3
CZZ-400	35.8	13.6	22.5	28.1	–	5.5:2.0:2.5
CZZ-500	34.5	13.5	23.4	28.6	–	5.4:2.0:2.6
CZZ-600	30.4	13.3	29.2	27.1	–	4.8:2.0:3.2

Table 3
XPS results for the samples of S-CZZ-300, S-CZZ-600, CZZ-300 and CZZ-600.

Catalyst	Relative surface concentration of metal (at.%)			Cu/Zn/Zr molar ratio
	Cu	Zn	Zr	
S-CZZ-300	43.5	41.0	15.5	4.4:4.1:1.5
S-CZZ-600	33.6	40.5	25.6	3.4:4.0:2.6
CZZ-300	62.0	23.0	15.0	6.2:2.3:1.5
CZZ-600	41.7	35.1	23.2	4.2:3.5:2.3

and peak β are almost the same over the two series samples calcined at the same temperatures. This result suggests that the addition of CTAB during the co-precipitation process has little effect on the basicity of the Cu–ZnO–ZrO_2 catalyst.

3.2. Catalytic performance

Activity and selectivity results for the methanol synthesis from CO_2 hydrogenation over the different Cu–ZnO–ZrO_2 catalysts are summarized in Table 5. CO and methanol are the only carbon-containing products under the present reaction conditions. From Table 5, it can be seen that with the elevation of calcination temperature of the S-CZZ and CZZ catalysts, the conversion of CO_2 decreases while the CH_3OH selectivity increases gradually. On the other hand, the yields of CH_3OH over the two series catalysts decrease with the increase in calcination temperature because the decreasing degree of the CO_2 conversion is larger than the increasing degree of the CH_3OH selectivity.

By comparing the catalytic performances of the two series catalysts S-CZZ and CZZ calcined at the same temperatures, we can note from Table 5 that the S-CZZ samples possess significantly higher methanol selectivity although with slightly lower CO_2 conversion; thus the yield of CH_3OH is enhanced remarkably compared with the corresponding CZZ samples.

Many studies have demonstrated that the activity of Cu-based catalysts for methanol synthesis from CO_2 hydrogenation is related closely to the metallic copper surface area (S_{Cu}) [7,9,12,15,55–57]. For example, some researchers report that there is a linear relationship between the methanol yield and the S_{Cu} of catalysts such as supported copper catalyst [55], Cu–ZnO–Al_2O_3 [56], Cu–ZnO modified with MO_x (M = Ga, Al, Zr, Cr) [12,57], and MO_x (M = B/Ga/In/Gd/Y/Mn/Mg) modified Cu–ZnO–ZrO_2 [7,9]. However, other researchers find out that it is not a linear relationship on the Cu–ZnO [58], Cu–ZnO–Al_2O_3 [59–62] and Cu–ZnO–ZrO_2 [31] catalysts. They suggest that S_{Cu} cannot be the only factor that determines the activity, and different particles sizes and interaction with support may greatly influence the activity as well

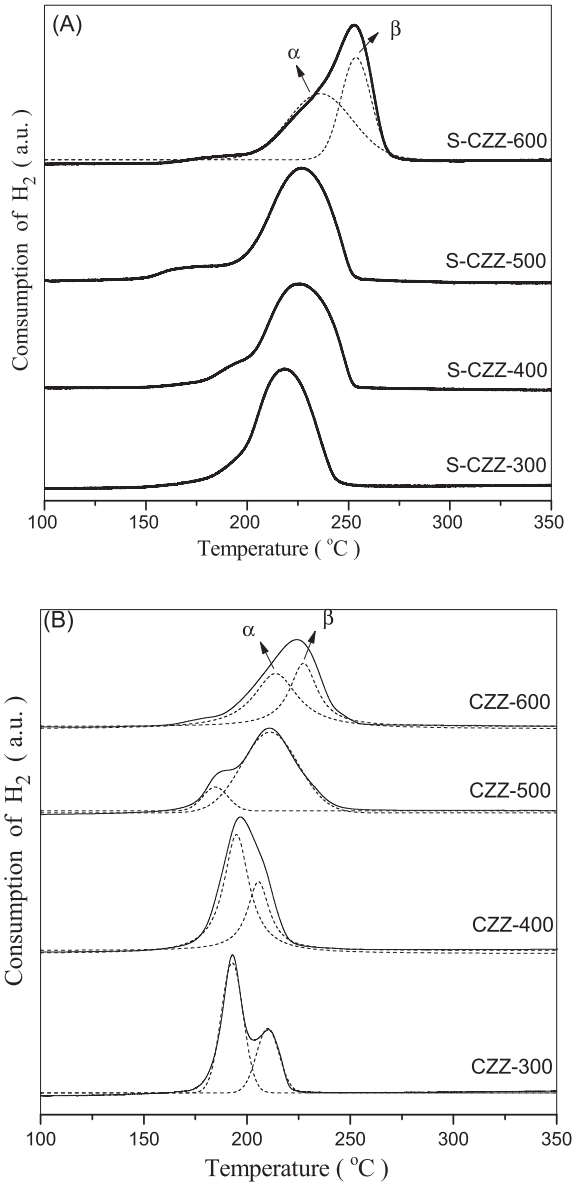

Fig. 7. H_2-TPR profiles of the different CuO–ZnO–ZrO_2 catalysts: (A) S-CZZ and (B) CZZ.

[61–63]. In the present study, as shown in Fig. 10, we find that the yields of methanol over the two series samples S-CZZ and CZZ increase with the increase of the S_{Cu} but they are not a linear relationship. On the other hand, the yields of methanol over the CZZ samples are significantly lower than those on the corresponding S-CZZ samples though with higher S_{Cu}. These results indicate that there must be other factors influencing the activity of the Cu–ZnO–ZrO_2 catalysts investigated here. This conclusion is consistent with that reported in the literature [61–63].

To better clarify this point, we calculate the turnover frequency (TOF) of methanol formation over the various catalysts and the results are presented in Table 5. It can be seen that the values of TOF varied in the range of $2.87–5.74 \times 10^{-3}$ s^{-1} and approximate values ($0.5–10.5 \times 10^{-3}$ s^{-1}) under similar reaction conditions were reported by other researchers [13]. Fig. 11 shows the relationship between the TOF values for methanol synthesis and the Cu particle sizes (d_{Cu}, Table 1) for the two series catalysts. Clearly, the TOF values decrease with the increase in d_{Cu} for the both series catalysts, although the decrease degree of the S-CZZ series catalysts is

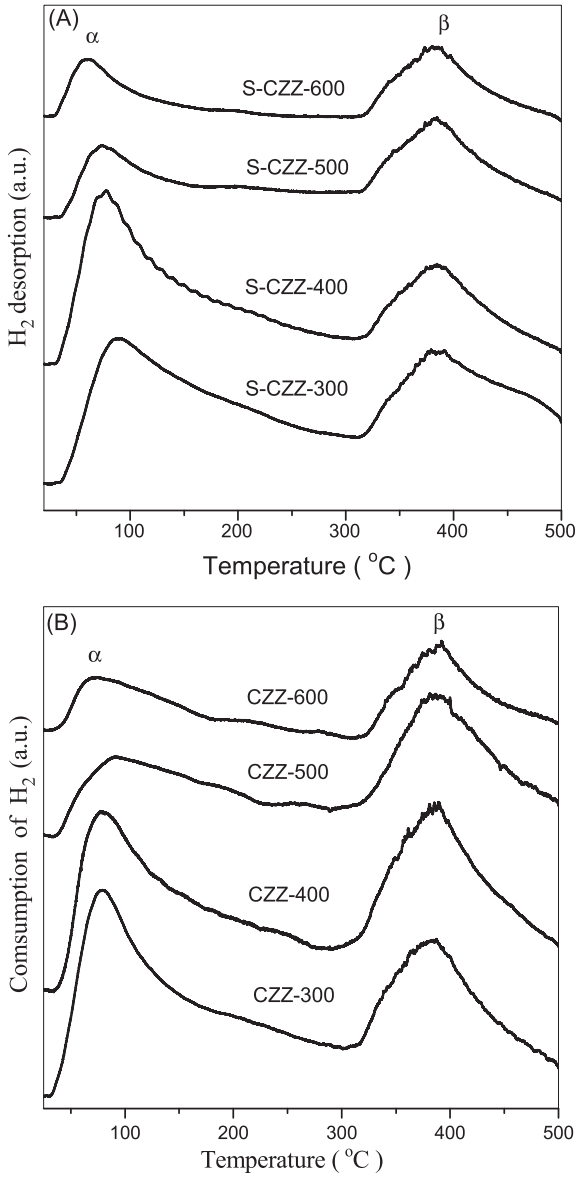

Fig. 8. H_2-TPD profiles of the reduced Cu–ZnO–ZrO_2 catalysts: (A) S-CZZ and (B) CZZ.

significantly larger than that of the CZZ series catalysts. The result is consistent with that reported by Koeppel et al. [60] on Cu/ZrO_2 catalyst and by Natesakhawat et al. [7] on CuZnZrGaY catalyst. These results indicate the structurally sensitive character of the title reaction and can be explained as follows:

(1) Comparing with larger particles, smaller crystallites usually have larger numbers of open planes, edge/defect sites containing coordinately unsaturated atoms which are more reactive than fully coordinated species. This has been confirmed by many experimental and computational studies on single-crystal surfaces, model and heterogeneous catalysts [7].
(2) It is well known that for the Cu-based catalysts for methanol synthesis, the catalytic activity depends greatly on the interaction between Cu and oxide components [61–63]. The intense interaction between Cu and oxide components is in favor of the formation of Cu–MO_χ (M = Zn and/or Zr) species which are suggested to exist at the Cu–MO_χ interface [64,65]. In conformity with this, some authors propose that the Cu–Zn [66] and Cu–Zr [60,67,68] sites are active sites for methanol synthesis from CO_2 hydrogenation on Cu–ZnO and Cu–ZrO_2-based catalysts, respectively. Evidently, smaller Cu particles can lead to larger interfacial area of the Cu–MO_χ interface, so resulting in higher activity. Similar viewpoint is also reported by Sun et al. [62] who found that the Cu species present in relative well-ordered crystalline and larger particle size will weaken the synergistic interaction between Cu and ZnO, so decreases the catalytic activity of the Cu–ZnO–Al_2O_3 catalyst.

It is worthy to note, however, that the TOF values of the CZZ series catalysts are evidently smaller than those of the corresponding S-CZZ series catalysts with the similar Cu particle sizes (Fig. 11), indicating that the TOF value for methanol formation is not simply dependent on the crystallite size of Cu [69]. From the catalytic activity data (Table 5) we can see that the smaller TOF values of the CZZ series catalysts compared with those of the corresponding S-CZZ series catalysts can be attributed to the much lower methanol selectivity. This result indicates that not all the copper area has the same specific activity for the two reactions, i.e. formations of methanol (Eq. (4)) and CO (Eq. (5)), respectively [51]. As discussed above, the Cu–ZnO_χ and/or the Cu–ZrO_χ interface are believed to be the main sites for methanol synthesis. [64,65]. However, CO formation is less sensitive to the kind of active site since the RWGS (Eq. (5)) reaction is a more facile reaction than the formation of methanol [51]. Even with the similar size of Cu particles, the S-CZZ series catalysts possess more Cu–ZnO_χ and/or Cu–ZrO_χ species, which can be evidenced by the TEM and EDX results. In contrast with the individual separated particles on the CZZ samples, the CuO particles are partially embedded in the oxide matrix with an intimate interface contact with the surrounding oxide on the S-CZZ samples. This special structure of the S-CZZ samples would possess more Cu–ZnO_χ and/or Cu–ZrO_χ species. Furthermore, this structure can inhibit the aggregation of metal copper during the reduction process, thus maintaining a large Cu–ZnO_χ and/or Cu–ZrO_χ interface. On the other hand, the more homogenous element distributions of the S-CZZ catalysts calcined at 300–500 °C compared with the corresponding CZZ catalysts as evidenced by the EDX result (Table 2) suggest that the catalysts prepared by the present surfactant-assisted co-precipitation method had a higher interdispersion of the metallic elements, which is beneficial for the formation of more Cu–ZnO_χ and/or Cu–ZrO_χ species [46]. Furthermore, as clarified by the pore size distributions shown in Fig. 4, the S-CZZ catalysts calcined at 300–500 °C possess mesoporous structures in contrast with the microporous structures of the corresponding CZZ catalysts. This mesoporous structure contributes to promote the migration and diffusion of the product molecules out of the pores, thus increasing the methanol selectivity due to the larger molecule diameter of methanol than that of CO. Similarly, a lesser extent of decrease in the TOF values of the CZZ-600 sample compared with the counterpart S-CZZ-600 can be ascribed to the same homogenous element distribution (Table 2) and to the possessing of mesoporous structure (Fig. 4).

$$CO_2 + 3H_2 \leftrightharpoons CH_3OH + H_2O\ \Delta H_{298} = -49.47\ \text{kJ/mol} \quad (4)$$

$$CO_2 + H_2 \leftrightharpoons CO + H_2O\ \Delta H_{298} = 41.17\ \text{kJ/mol} \quad (5)$$

Table 4
Temperatures (T_{max}) and desorption areas of H_2-TPD profiles of the reduced Cu–ZnO–ZrO_2 catalysts.

Catalyst	α Peak		β Peak	
	T_α (°C)	A_α (a.u.)	T_β (°C)	A_β (a.u.)
S-CZZ-300	86	354	382	178
S-CZZ-400	79	350	383	154
S-CZZ-500	75	130	383	147
S-CZZ-600	72	81	385	137
CZZ-300	78	357	385	179
CZZ-400	73	352	382	195
CZZ-500	74	199	385	183
CZZ-600	72	101	386	139

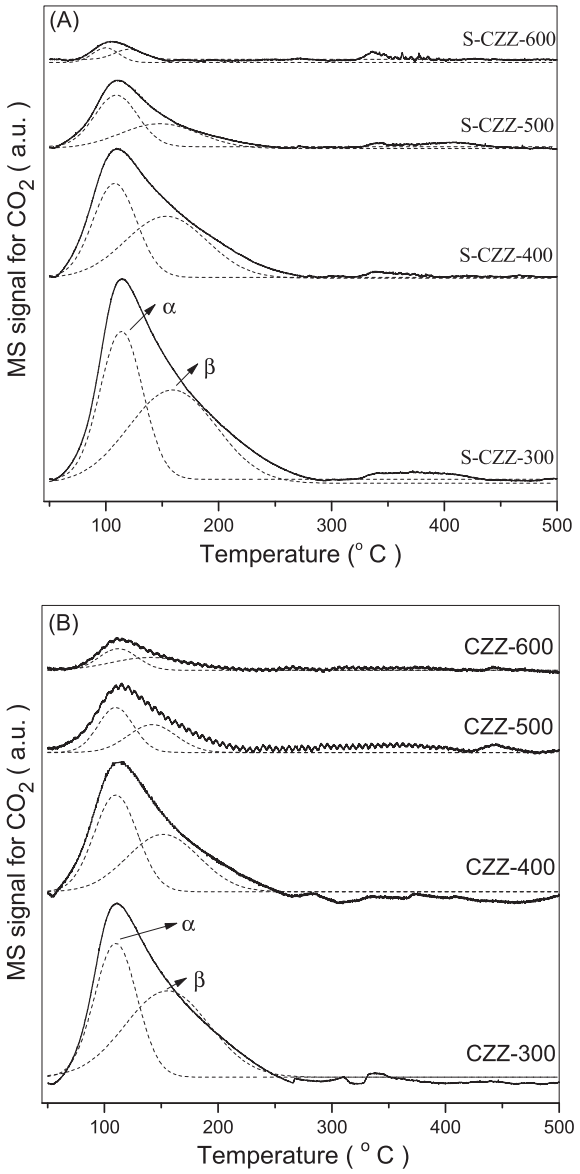

Fig. 9. CO_2-TPD profiles of the reduced Cu–ZnO–ZrO_2 catalysts: (A) S-CZZ and (B) CZZ.

4. Conclusions

A series of CuO–ZnO–ZrO_2 catalysts with narrow mesopores size distributions were prepared via a surfactant-assisted co-precipitation method. The methanol yield decreases with the increase in calcination temperature of the catalyst, which can be attributed to the decrease in TOF for methanol formation due to the enlargement of Cu particles. Methanol synthesis from CO_2 hydrogenation is a structure-sensitive reaction with smaller Cu particles demonstrating high TOF values. Compared with the catalysts of the same composition prepared by the conventional co-precipitation method, the mesoporous CuO–ZnO–ZrO_2 catalysts exhibit an evidently high methanol selectivity, which can be attributed to the formation of more Cu–ZnO_χ and/or Cu–ZrO_χ species and mesoporous structures.

Table 5
Catalytic performance of the different Cu–ZnO–ZrO_2 catalysts.

Catalyst	CO_2 conv. (%)	CH_3OH sel. (%)	CH_3OH yield (%)	TOF of $CH_3OH \cdot 10^3$ (S^{-1})
S-CZZ-300	12.1	54.1	6.5	5.74
S-CZZ-400	11.0	55.4	6.1	5.43
S-CZZ-500	9.3	58.9	5.5	4.89
S-CZZ-600	4.8	73.4	3.5	3.40
CZZ-300	14.3	32.5	4.6	3.10
CZZ-400	11.7	33.2	3.9	3.06
CZZ-500	10.4	36.5	3.8	2.99
CZZ-600	8.1	38.6	3.1	2.87

Reaction conditions: $H_2/CO_2 = 3$, T = 240 °C, P = 3.0 MPa, GHSV = 3600 h^{-1}.
Experimental errors of the CO_2 conversion and CH_3OH selectivity are within ±3%.

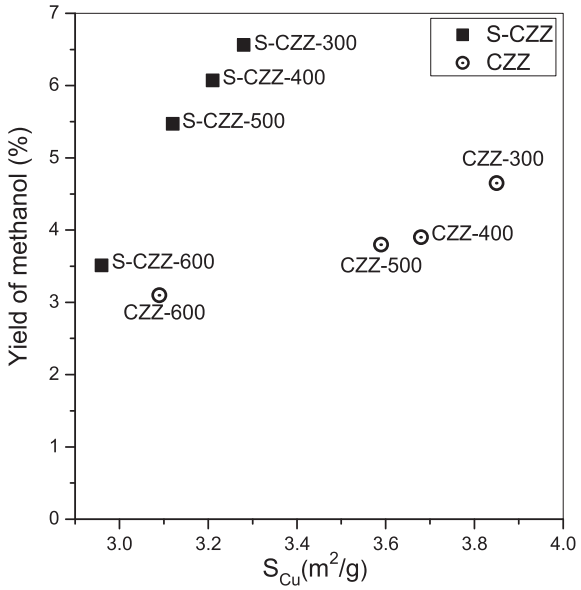

Fig. 10. The relationship between the yield of methanol and the Cu surface area. Reaction conditions: $H_2/CO_2 = 3$, T = 240 °C, P = 3.0 MPa, GHSV = 3600 h^{-1}.

Acknowledgements

The authors thank Shanghai Municipal Education Commission (13YZ117) and Science and Technology Commission of Shanghai Municipality (13ZR1441200) for financial support. The authors wish to express their great appreciation to Prof. Yong Cao from Department of Chemistry, Fudan University, for his fruitful discussion and adequate suggestions.

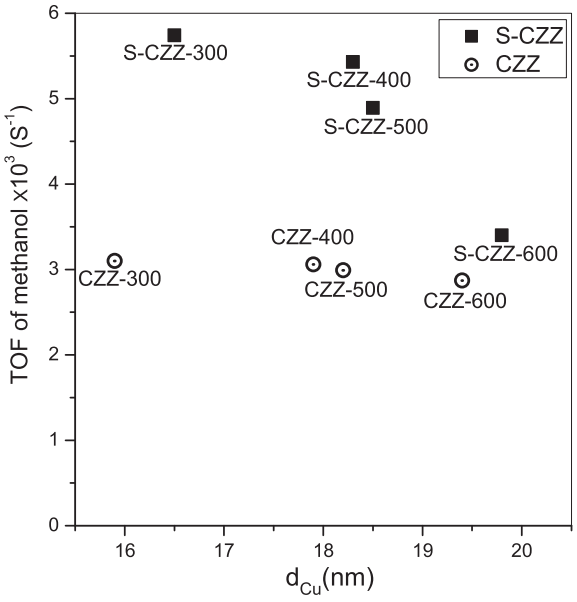

Fig. 11. The relationship between the TOF of methanol and Cu particle size. Reaction conditions: $H_2/CO_2 = 3$, T = 240 °C, P = 3.0 MPa, GHSV = 3600 h^{-1}.

References

[1] W. Wang, S.P. Wang, X.B. Ma, J.L. Gong, Chem. Soc. Rev. 40 (2011) 3703–3727.
[2] G.A. Olah, Angew. Chem. Int. Ed. 44 (2005) 2636–2639.
[3] G.A. Olah, Angew. Chem. Int. Ed. 52 (2013) 104–107.
[4] K. Fujimoto, Y. Yu, Stud. Surf. Sci. Catal. 77 (1993) 393–396.
[5] F. Arena, K. Barbera, G. Italiano, G. Bonura, L. Spadaro, F. Frusteri, J. Catal. 249 (2007) 185–194.
[6] C.M. Li, X.D. Yuan, K. Fujimoto, Appl. Catal. A Gen. 469 (2014) 306–311.
[7] S. Natesakhawat, J.W. Lekse, J.P. Baltrus, P.R. Ohodnicki Jr., B.H. Howard, X.Y. Deng, C. Matranga, ACS Catal. 2 (2012) 1667–1676.
[8] Y. Ma, Q. Sun, D. Wu, W.H. Fan, Y.L. Zhang, J.F. Deng, Appl. Catal. A Gen. 171 (1998) 45–55.
[9] J. Słoczyński, R. Grabowski, P. Olszewski, A. Kozłowska, J. Stoch, M. Lachowska, J. Skrzypek, Appl. Catal. A Gen. 310 (2006) 127–137.
[10] J. Sloczynski, R. Grabowski, A. Kozlowska, M. Lachowska, J. Skrzypek, Stud. Surf. Sci. Catal. 153 (2004) 161–164.
[11] R. Raudaskoski, M.V. Niemelä, R.L. Keiski, Top. Catal. 45 (2007) 57–60.
[12] M. Saito, T. Fujitani, M. Takeuchi, T. Watanabe, Appl. Catal. A Gen. 138 (1996) 311–318.
[13] J. Sloczyński, R. Grabowski, A. Kozłowska, P. Olszewski, J. Stoch, J. Skrzypek, M. Lachowska, Appl. Catal. A Gen. 278 (2004) 11–23.
[14] F. Arena, G. Italiano, K. Barbera, S. Bordiga, G. Bonura, L. Spadaro, F. Frusteri, Appl. Catal. A Gen. 350 (2008) 16–23.
[15] F. Arena, G. Italiano, K. Barbera, G. Bonura, L. Spadaro, F. Frusteri, Catal. Today 143 (2009) 80–85.
[16] R. Raudaskoski, E. Turpeinen, R. Lenkkeri, E. Pongrácz, R.L. Keiski, Catal. Today 144 (2009) 318–323.
[17] F. Arena, G. Mezzatesta, G. Zafarana, G. Trunfio, F. Frusteri, L. Spadaro, J. Catal. 300 (2013) 141–151.
[18] R. Ladera, F.J. Pérez-Alonso, J.M. González-Carballo, M. Ojeda, S. Rojas, J.L.G. Fierro, Appl. Catal. B Eviron 142–143 (2013) 241–248.
[19] J. Słoczyński, R. Grabowski, A. Kozłowska, P. Olszewski, M. Lachowska, J. Skrzypek, J. Stoch, Appl. Catal. A Gen. 249 (2003) 129–138.
[20] M. Lachowska, J. Skrzypek, React. Kinet. Catal. Lett. 83 (2004) 269–273.
[21] Y. Cong, K.C. Tin, N.B. Wang, C.H. Xu, T. Zhang, X.Y. Sun, W. Guan, D.B. Liang, Chin. J. Catal. 21 (2000) 247–250.
[22] Y. Cong, X.H. Bao, T. Zhang, X.Y. Sun, D.B. Liang, K.C. Tin, N.B. Wang, Chin. J. Catal. 21 (2000) 314–318.
[23] H.J. Zhan, F. Li, P. Gao, N. Zhao, F.K. Xiao, W. Wei, L.S. Zhong, Y.H. Sun, J. Power Sources 251 (2014) 113–121.
[24] H.Y. Ban, C.M. Li, K. Asami, K. Fujimoto, Catal. Commun. 54 (2014) 50–54.
[25] G. Bonura, F. Arena, G. Mezzatesta, C. Cannilla, L. Spadaro, F. Frusteri, Catal. Today 171 (2011) 151–156.
[26] G. Bonura, M. Cordaro, C. Cannilla, F. Arena, F. Frusteri, Appl. Catal. B Environ. 152–153 (2003) 152–161.
[27] E. Frei, A. Schaadt, T. Ludwig, H. Hillebrecht, I. Krossing, ChemCatChem 6 (2014) 1721–1730.
[28] X.M. Guo, D.S. Mao, G.Z. Lu, S. Wang, G.S. Wu, Catal. Commun. 10 (2009) 1661–1664.
[29] X.M. Guo, D.S. Mao, G.Z. Lu, S. Wang, G.S. Wu, J. Catal. 271 (2010) 178–185.
[30] X.M. Guo, D.S. Mao, G.Z. Lu, S. Wang, Acta Phys. Chim. Sin. 28 (2012) 170–176.
[31] X.M. Guo, D.S. Mao, G.Z. Lu, S. Wang, G.S. Wu, Catal. Commun. 12 (2011) 1095–1098.
[32] F.L. Liao, Y.Q. Huang, J.W. Ge, W.R. Zheng, K. Tedsree, P. Collier, X.L. Hong, S.C. Tsang, Angew. Chem. Int. Ed. 50 (2011) 2162–2165.
[33] M.F. Luo, J.M. Ma, J.Q. Lu, Y.P. Song, Y.J. Wang, J. Catal. 246 (2007) 52–59.
[34] L. Qi, Q. Yu, Y. Dai, C.J. Tang, L.J. Liu, H.L. Zhang, F. Gao, L. Dong, Y. Chen, Appl. Catal. B Environ. 119–120 (2012) 308–320.
[35] Z. Wang, Z.P. Qu, X. Quan, Z. Li, H. Wang, R. Fan, Appl. Catal. B Environ. 134–135 (2013) 153–166.
[36] X.D. Ma, X. Feng, X. He, H.G. Guo, L. Lv, J. Guo, H.Q. Cao, T. Zhou, Microporous Mesoporous Mater. 158 (2012) 214–218.
[37] J.L. Cao, Y. Wang, X.L. Yu, S.R. Wang, S.H. Wu, Z.Y. Yuan, Appl. Catal. B Environ. 79 (2008) 26–34.
[38] J.L. Cao, Y. Wang, T.Y. Zhang, S.H. Wu, Z.Y. Yuan, Appl. Catal. B Environ. 78 (2008) 120–128.
[39] J. Huang, Y.F. Kang, L.W. Wang, T.L. Yang, Y. Wang, S.R. Wang, Catal. Commun. 15 (2011) 41–45.
[40] J. Huang, Y.F. Kang, T.L. Yang, Y. Wang, S.R. Wang, React. Kinet. Mech. Catal. 104 (2011) 149–161.
[41] G.C. Chinchen, C.M. Hay, H.D. Vandervell, K.C. Waugh, J. Catal. 103 (1987) 79–86.
[42] E.D. Batyrev, J.C. van den Heuvel, J. Beckers, W.P.A. Jansen, H.L. Castricum, J. Catal. 229 (2005) 136–143.
[43] Z.Y. Yuan, B.L. Su, Chem. Phys. Lett. 381 (2003) 710–714.
[44] T.Z. Ren, Z.Y. Yuan, B.L. Su, Chem. Phys. Lett. 374 (2003) 170–175.
[45] M. Behrens, A. Furche, I. Kasatkin, A. Trunschke, W. Busser, M. Muhler, B. Kniep, R. Fischer, R. Schlögl, ChemCatChem 2 (2010) 816–818.
[46] J. Bao, Z.L. Liu, Y. Zhang, N. Tsubaki, Catal. Commun. 9 (2008) 913–918.
[47] I. Melián-Cabrera, M. López Granados, J.L.G. Fierro, J. Catal. 210 (2002) 273–284.
[48] N.F.P. Ribeiro, M.M.V.M. Souza, M. Schmal, J. Power Sources 179 (2008) 329–334.
[49] Y.P. Zhang, J.H. Fei, Y.M. Yu, X.M. Zheng, Energy Convers. Manage 47 (2006) 3360–3367.
[50] G. Avgouropoulos, T. Ioannides, H. Matralis, Appl. Catal. B Environ. 56 (2005) 87–93.
[51] K.W. Jun, W.J. Shen, K.S.R. Rao, K.W. Lee, Appl. Catal. A Gen. 174 (1998) 231–238.
[52] M.G. Lin, C. Yang, G.S. Wu, W. Wei, W.H. Li, Y.K. Shan, Y.H. Sun, M.Y. He, Chin. J. Catal. 25 (2004) 591–595.
[53] D. Bianchi, J.L. Gass, M. Khalfallah, S.J. Teichner, Appl. Catal. A Gen. 101 (1993) 297–315.
[54] L.X. Zhang, Y.C. Zhang, S.Y. Chen, Appl. Catal. A Gen. 415–416 (2012) 118–123.
[55] B. Denise, R.P.A. Sneeden, B. Beguin, O. Cherifi, Appl. Catal. 30 (1987) 353–363.
[56] G.C. Chinchen, M.S. Spencer, Catal. Today 10 (1991) 293–301.
[57] M. Saito, T. Fujitani, I. Takahara, T. Watanabe, M. Takeuchi, Y. Kanai, K. Moriya, T. Kakumoto, Energ. Convers. Manag. 36 (1995) 577–580.
[58] G.C. Chinchen, K.C. Waugh, D.A. Whan, Appl. Catal. 25 (1986) 101–107.
[59] G.C. Chinchen, P.J. Denny, D.G. Parker, M.S. Spencer, D.A. Whan, Appl. Catal. 30 (1987) 333–338.
[60] R.A. Koeppel, A. Baiker, Ch Schild, A. Wokaun, Stud. Surf. Sci. Catal. 63 (1991) 59–68.
[61] T. Witoon, T. Permsirivanich, W. Donphai, A. Jaree, M. Chareonpanich, Fuel Process. Technol. 116 (2013) 72–78.
[62] Q. Sun, Y.L. Zhang, H.Y. Chen, J.F. Deng, D. Wu, S.Y. Chen, J. Catal. 167 (1997) 92–105.
[63] D.J. Wang, J. Zhao, H.L. Song, L.J. Chou, J. Nat. Gas Chem. 20 (2011) 629–634.
[64] J.D. Grunwaldt, A.M. Molenbroek, N.Y. Topsøe, H. Topsøe, B.S. Clausen, J. Catal. 194 (2000) 452–460.
[65] F.L. Liao, Z.Y. Zeng, C. Eley, Q. Lu, X.L. Hong, S.C.E. Tsang, Angew. Chem. Int. Ed. 51 (2012) 5832–5836.
[66] T. Fujitani, J. Nakamura, Appl. Catal. A Gen. 191 (2000) 111–129.
[67] R.A. Koeppel, A. Baiker, A. Wokaun, Appl. Catal. A Gen. 84 (1992) 77–102.
[68] J.Y. Liu, J.L. Shi, D.H. He, Q.J. Zhang, X.H. Wu, Y. Liang, Q.M. Zhu, Appl. Catal. A Gen. 218 (2001) 113–119.
[69] S. Fujita, Y. Kanamori, A.M. Satriyo, N. Takezawa, Catal. Today 45 (1998) 241–244.